Permeability of wormholes created by CO_2-acidized water flow through stressed carbonate rocks

A. P. S. Selvadurai,[a] Cyrille-B. Couture, and S. M. Rezaei Niya
Environmental Geomechanics Laboratory, Department of Civil Engineering and Applied Mechanics, McGill University, Montréal, Quebec H3A 0C3, Canada

(Received 17 May 2017; accepted 28 August 2017; published online 26 September 2017)

Sequestration of CO_2 relies on the storage capabilities of the deep geologic setting throughout the lifetime of the storage activity. Preferred storage horizons are largely composed of sandstone, which is considered to be chemically inert to the injected CO_2. Carbonate rocks and carbonate zones existing as seams or lenses in sandstone formations are, however, prone to chemical alteration during reactive flows of CO_2-acidized water that can be created by the mixing of the injected CO_2 with either fresh or saline water present in a storage horizon. Reactive flows can erode the fabric of carbonate rocks leading to the creation of high permeability pathways that are referred to as *wormholes*. The paper first examines the generation of wormholes in cylindrical samples of calcium carbonate-rich Indiana Limestone that are subjected to *geostatic stress states* representative of deep sequestration sites. The leakage potential of the wormhole is examined by appeal to computational fluid dynamics simulations of Stokes' flow in wormhole features and an elementary approach involving Stokes' flow-based hydraulic diameter concept in cylindrical pathways with deviating segments, representing the passages for flow in a wormhole. *Published by AIP Publishing.* https://doi.org/10.1063/1.5002129

I. INTRODUCTION

The concept of geologic sequestration of CO_2 relies on several trapping mechanisms to provide storage security and its longevity.[1–5] The primary trapping mechanisms commonly identified include adsorption, structural, stratigraphic, and hydrodynamic trapping, which are activated at the time of sequestration and can continue for several hundred years. Secondary trapping mechanisms, including dissolution and mineralization, offer a degree of permanence to the sequestration process but may require time scales in excess of a thousand years[1] and very much depend on the effectiveness of the primary trapping mechanisms.

The failure of the caprock to effectively trap the injected fluid can result in CO_2 leakage to the surficial formations and subsequently to the atmosphere, making the sequestration exercise ineffective. Natural analogues of CO_2 migration from deep volcanic sources have been reported in the literature, as has the role of abandoned wells and geological conduits in enhancing leakage.[1–3] Leakage of CO_2 has also occurred through natural fractures and a signature of the leakage is evidenced by dead vegetation similar to that observed at the Mammoth Mountain site, California.[6] The security and longevity of the caprock barrier is therefore central to the geologic sequestration of CO_2. One article of interest[7] discusses several important issues related to the impact of geochemical reactions on multiphasic transport processes and the overall implications on the sequestration strategy.

The role of geomechanics is particularly important when considering the injection of large volumes of fluidized CO_2[8–15] into storage reservoirs; movement of faults and dormant fractures that may be triggered by the pressurization can have major implications in the definition of *secure geologic sequestration*. Defects created by the dissolution of carbonate rocks can have adverse effects on the sequestration activity by (i) creating direct flow paths (dissolution channels and wormholes) through the caprock, (ii) compromising the integrity of the impervious caprock or confining layer by creating strength reduction zones in the reservoir that can trigger wormhole collapse, and (iii) inhibiting capillary trapping by short-circuiting the efficient use of the entire storage domain, creating high permeability zones dominated by wormhole cavities in carbonate seams and lenses (Fig. 1).

Currently, many storage settings rely on the chemical inertness of the storage formation rocks that are predominantly sandstone in composition.[3] The presence of carbonate zones can, however, localize the chemical dissolution and mineral transport, which can alter the geomechanical and sequestration properties of the reservoir. Efforts have been made to examine the influence of dissolution that can occur when CO_2-acidized flow takes place in carbonate rocks. Studies of dissolution and precipitation of reactive minerals during CO_2-acidized water flow through Indiana Limestone and St. Andres Limestone are reported in Ref. 7.

Several laboratory-scale studies[16–23] have clearly established the development of wormhole-type features in carbonate rocks exposed to CO_2-acidized flow. These studies are largely experimental and make no attempt to examine the fluid dynamics aspects of the wormhole itself, with a view to defining the permeability characteristics of the wormhole. The current experiments were performed on isotropically stressed samples and the influences of anisotropic geostatic stress states are examined only in a limited number of studies.[13,18,22]

[a]E-mail: patrick.selvadurai@mcgill.ca. Tel.: +1 514 398 6672. Fax: +1 514 398 7361.

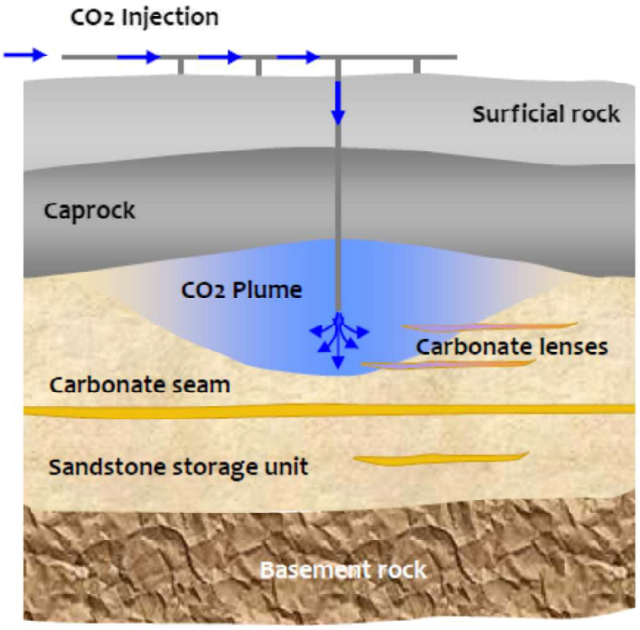

FIG. 1. A geologic sequestration scenario—interaction of a migrating CO_2 plume with carbonate lenses. This schematic view shows carbonate lenses that can be present in a predominantly sandstone storage horizon. The injected CO_2 in a fluidized form can combine with groundwater to create conditions that are simulated in the experiments.

The basic objective of this research is to further investigate the dissolution mechanism resulting from the interaction of CO_2-acidized water with reactive rocks and its relation to the geomechanical stress states that can exist when CO_2-acidized flow takes place through cylindrical cores of Indiana Limestone. In the context of this research, the term CO_2-acidized flow refers to the flow of a mixture of CO_2 and water that is maintained and delivered to the sample at a specified pH value (between 3 and 4). Once a wormhole is generated, the important issue in relation to the geologic sequestration is to establish the potential for leakage from the defect, which is the justification for examining the flow characteristics of wormholes.

II. EXPERIMENTAL TECHNIQUES

A. Stress state

To examine the effects of CO_2 injection on *stressed rocks* in a laboratory setting, CO_2-acidized water flow experiments were conducted on cylindrical cores of the predominantly carbonate Indiana Limestone (IL), measuring 50 mm diameter and 100 mm in length. For purposes of comparison, experiments were also conducted on the predominantly quartzitic Rudna Sandstone (RS). The samples were injected with CO_2-acidized water, in the presence of a triaxial stress state. In the first series of experiments, three samples of IL and one sample of RS were tested under an isotropic stress or a cell pressure of 10 MPa. In a second series of experiments, three additional samples of IL were tested at a triaxial stress state corresponding to an *isotropic stress* of 10 MPa and a *deviator stress* of 20 MPa. The *deviator stress* is defined by

$$\sigma_{deviator} = \sigma_1 - \sigma_3, \quad (1)$$

where σ_1 is the maximum principal stress and σ_3 is the minimum principal stress. In a conventional triaxial test, the sample is first subjected to an all round compressive stress σ_3. The axial stress applied through the piston is the deviator stress, which corresponds to $(\sigma_1 - \sigma_3)$. Because of the axial symmetry of the stress state to which the sample is subjected, only two of the three principal stresses are present. This is in keeping with geostatic stress states, where the gravitational stresses generally give rise to the maximum principal stress in the vertical direction, and the minimum principal stresses, which are usually equal, act in the horizontal plane orthogonal to the gravitational direction. On occasions, large tectonic actions can result in the maximum principal stresses acting in the horizontal plane and, in such situations, there can be three unequal principal stresses. In this research, however, the cylindrical rock sample is subjected to a major principal stress σ_1 and a minor principal stress σ_3. The deviator stress state applied was representative of typical stress states that can be encountered at actual and potential sequestration settings.[24]

B. The CO_2-acidized water

The CO_2-acidized water was created in a continuously stirred autoclave by mixing filtered water with liquid CO_2 maintained at a pressure of 8 MPa and at a temperature between 24.4 °C and 26.2 °C for a minimum of 12 h.[25] During the experiment, as filtered water was pumped into the autoclave and, due to the incompressible nature of the fluid mixture, an equal volume of CO_2-acidized water was delivered to the sample in the triaxial cell. The large residence time and rapid dissociation of dissolved CO_2 into bicarbonate and carbonate ions ensured that the composition of the reactive fluid remained relatively uniform. The pH of the CO_2-acidized water was estimated using a colour graded pH indicator paper contained in a specially fabricated inspection chamber. This experiment was performed separately in order to minimize interactions with the primary experiment. The pH was estimated to be between 3 and 4.

C. Test procedure

A schematic view of the experimental arrangements is given in Fig. 2 and a photographic view of the test facilities is shown in Fig. 3. At the start of each experiment, water was pumped into the sample while a backpressure regulator located at the outlet from the high pressure triaxial cell (Fig. 2) was adjusted until the pore pressure in the sample was equal to the pressure within the autoclave (8 MPa). The fluid flow was then redirected to the autoclave using a system of valves and set to a constant rate of 1 ml/min for the duration of the test. Pressure transducers were used to monitor any changes in the inlet and outlet fluid pressures and the temperature of the fluid in the autoclave was measured using type K thermocouples. The data from the various transducers were recorded every second to detect any abrupt variations. The recorded experimental data were used to estimate the permeability evolution during a 24 h period.

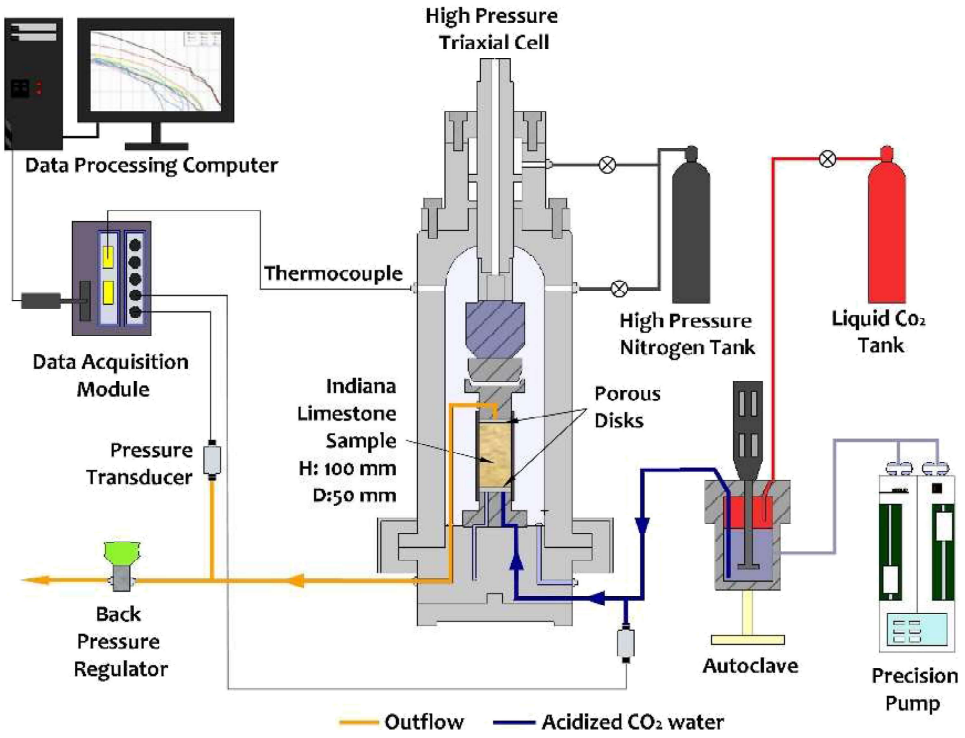

FIG. 2. A schematic view of the test arrangement for initiating CO_2-acidized flow through the rock samples.

III. EXPERIMENTAL RESULTS

A. Permeability evolution

During the experiments, the CO_2-acidized water migrating through the IL samples reacted with the carbonate minerals, resulting in rapid dissolution of the carbonate matrix. The dissolved minerals were transported by the advecting fluid and precipitated in the backpressure regulator located at the outlet. Degassing enhanced the fluid flow through the IL samples, which lead to a measurable decrease in the upstream pressure needed to maintain the controlled fluid flow rate. In contrast, the Rudna Sandstone samples showed no evidence of permeability alteration during migration of the CO_2-acidized water through its pore space. Assuming that the flow domain remained unchanged until breakthrough occurred (i.e., the created wormhole formed the primary pathway for fluid migration), Darcy's law was used to estimate the permeability evolution in the sample: i.e.,

$$K = \frac{\mu Q L}{A_0 \Delta p}, \tag{2}$$

where K is the permeability (m^2), μ is the dynamic viscosity of the fluid (Pa s), Q is the flow rate (m^3/s), L is the length of the sample (m), A_0 is the gross cross-sectional area of the sample (m^2), and Δp is the pressure differential across the sample (Pa). In (2), the implicit assumption is that Darcy's law can be formulated in terms of the spatially averaged velocity and the *gross cross sectional area*. The time-dependent evolution of the *apparent permeability* for all the experiments is shown in Fig. 4. At this point, the following comment should be noted: the calculation of the permeability of the cylindrical specimen experiencing chemically induced erosion and wormhole development uses the initial cross-sectional area of the specimen in order to provide a normalized cross sectional area applicable to both intact and reacted samples. In reality, the result (2) is completely valid for the unreacted cylindrical specimen but this will not adequately reflect the evolution of the zones through which the flow will take place as the carbonate rock is progressively eroded by the CO_2-acidized water. In order to develop a measure of permeability in a continuously evolving wormhole, an X-Ray Tomography (X-RT) technique that is capable of tracking the wormhole pattern with time should be used. Such a facility is non-routine and it is a costly experimental technique, particularly when testing is carried out at high cell pressures and at large values of deviatoric stress states. Upon exposure to CO_2-acidized water, and the development of breakthrough (Fig. 4), the predominant zone through which

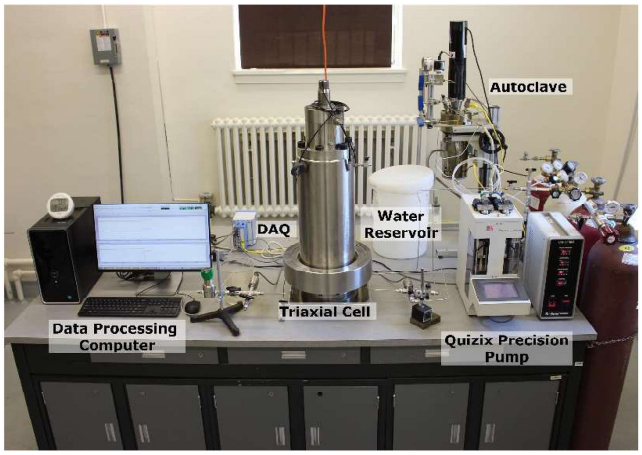

FIG. 3. The experimental facilities for performing CO_2-acidized flow through carbonate rocks.

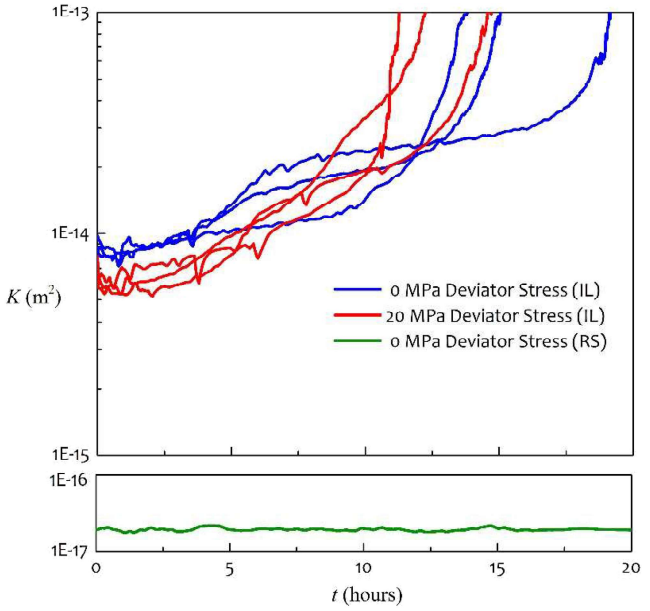

FIG. 4. Time history of permeability variation (sample cross-sectional area: 1963 mm^2). During steady state flow of CO_2-acidized water, the dissolution of calcite in Indiana Limestone (IL) resulted in an increase in permeability, whereas Rudna Sandstone (RS) exhibited no significant change in permeability over the same time period. The initial permeability of the IL samples varied between 6.1×10^{-15} m^2 and 9.8×10^{-15} m^2.

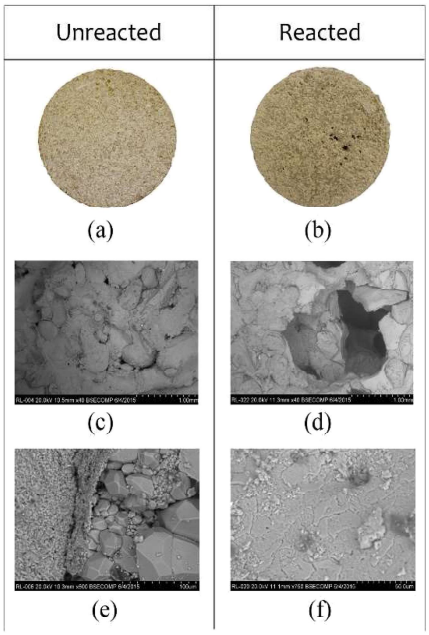

FIG. 5. Surface appearance of Indiana Limestone. The 50 mm diameter virgin inlet surface (a) shows no sign of defects compared to the reacted inlet surface (b) where multiple localized cavities are visible. The SEM images of the unreacted surface at 40× magnification (c) and 500× magnification (e) emphasize the various calcite mineral sizes present in the natural formation. The SEM images of the reacted surface cavity at a magnification of 40× (d) and 750× (f) show the uneven dissolution of the calcite minerals and removal of larger grains due to erosion of the matrix.

the CO_2-acidized flow takes place is the wormhole region, and the effective area of flow can be estimated by considering the overall volume of the wormhole and the length of the sample. Following the series of CO_2-acidized flow experiments, one sample was tested in a one-dimensional steady state apparatus,[26] which provides a low system resistance environment, resulting in a more accurate measurement of the permeability of the wormhole with low differential pressures. The six identical IL samples were tested at the same conditions of temperature, pore fluid pressure, and with the percolating fluid maintained at the observed pH range. Thus, for the two cases investigated and shown in the upper section of Fig. 4, only the stress state was varied according to the procedure described in Sec. II A. The results indicate an average increase in effective permeability of the six samples from 8.7×10^{-15} m^2 (unreacted state) to 3.6×10^{-12} m^2 (exposure to CO_2-acidized water flow). The deviatoric stress used in the experiments is typical of stress states that can be encountered at sequestration depths. The effect of the deviatoric stress on the wormhole development during CO_2-acidized flow, however, is not markedly noticeable due to the large dispersion of data from the three experiments repeated at each stress state. In this study, the influence of the mechanical variables, notably the stress state, was not considered in the computational modeling exercises involving fluid dynamics in fully developed wormholes. The inclusion of such effects will be important when examining the influence of long term transient processes involving coupled thermo-hydro-mechanical effects.[27]

B. Wormhole development

The Indiana Limestone samples subjected to CO_2-acidized flow showed significant signs of defect development at the entry surface and nominal effects at the exit surface (Fig. 5). Scanning Electron Microscope (SEM) images were used to identify the post-CO_2 exposure defects at the inlet surface of an IL sample; for purposes of reference, SEM images of a virgin cleaved IL surface were also taken. The images shown in Fig. 5 compare the pore scale features of the virgin Indiana Limestone with the surface topography observed near the inlet location of the wormhole. To observe details of the dissolution pattern created within the Indiana Limestone during CO_2 acidized flow, X-RT scans were performed on all the samples. These were reconstructed to develop three-dimensional replicas of the wormholes. The wormhole wall boundary was estimated by selecting a threshold on the gray scale value of each voxel, calibrated using cavities of known dimensions. From the image reconstruction (Fig. 6), it also appears that the rapid fluid velocity in the pore space and the high partial pressure of CO_2 in solution promoted the development of a *wormhole of the conical* variety.[20,28] Furthermore, the experimental results clearly suggest that once a dissolution region has been nucleated, that region will serve as a wormhole generator leading to the acidized-dissolution that ultimately creates a single dominant wormhole.[29]

IV. COMPUTATIONAL MODELING

Ideally, multiphysics simulations of Thermo-Hydro-Mechanical-Chemical (THMC) processes should map the time-dependent evolution of a wormhole as acidized CO_2-induced dissolution takes place; the current experimental

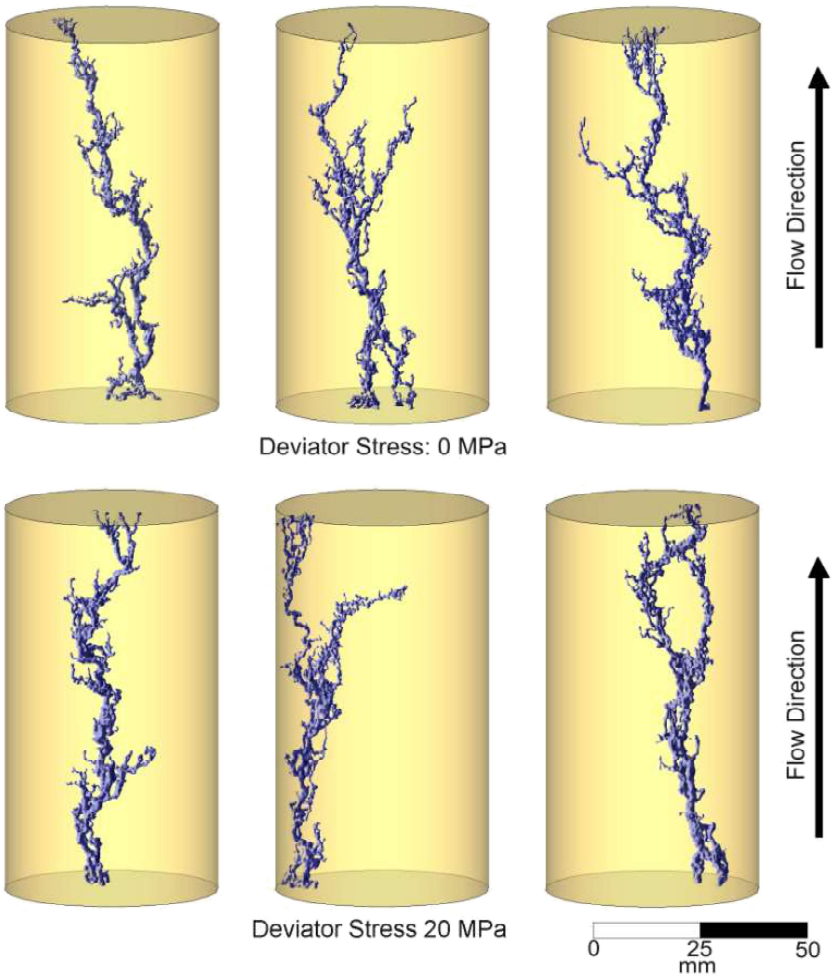

FIG. 6. X-ray tomography images of wormholes developed in Indiana Limestone. The size of the wormholes ranges between 538 mm^3 and 646 mm^3 and their geometry varies significantly, although tested under similar conditions. There is no visual evidence to suggest that the deviator stress influences the size or development of wormholes.

facilities cannot adequately address this issue because experimental facilities for tracking wormhole evolution require active and continuous X-RT imaging in a high pressure environment. Changes in permeability over time cannot uniquely identify the geometry of the wormhole. 3D fluid dynamics simulations were conducted to characterize the permeability of a wormhole; such results have greater practical utility because leakage from wormholes is important for assessing sequestration efficiency. To examine the permeability properties of a wormhole, the fluid movement within a selected X-RT-imaged wormhole was modelled using the steady state Stokes' flow equations of incompressible fluid dynamics.[30–32] The ABAQUS™finite element code was used to solve the governing partial differential equations,

$$\nabla \cdot \mathbf{v} = 0, \tag{3}$$

$$\nabla p = \mu \nabla^2 \mathbf{v}, \tag{4}$$

where $\mathbf{v}(\mathbf{x})$ is the velocity vector, $p(\mathbf{x})$ is the fluid pressure, ∇ is the gradient operator, ∇^2 is Laplace's operator, μ the dynamic viscosity of the fluid, and $\mathbf{x}$ is the position vector. Boundary conditions are specified on the inlet (S_i) and outlet (S_o) surfaces of the wormhole and at the interface between the wormhole surface and the rock (S_w), i.e.,

$$p(\mathbf{x}) = p_i, \quad \mathbf{x} \in S_i, \tag{5}$$

$$p(\mathbf{x}) = p_o, \quad \mathbf{x} \in S_o, \tag{6}$$

$$\mathbf{v}(\mathbf{x}) = 0, \quad \mathbf{x} \in S_w. \tag{7}$$

Equations (5) and (6) correspond, respectively, to the constant pressure boundary conditions at the inlet and outlet surfaces of the wormhole, and Eq. (7) correspond to the non-slip boundary condition along the walls of the wormhole. The parameters used were identical to those employed in the interpretation of the experimental results; at an average temperature of 24.4 °C, the dynamic viscosity and density were assumed to be 9.11×10^{-4} Pa s and 997 kg/m^3, respectively.[33] Visual representations of the fluid velocity distributions in regions of the wormhole are shown in Fig. 7. An alternative approach is to formulate the problem of flow through the wormhole as a transient problem in computational fluid dynamics that requires the solution of the complete non-linear form of the Navier-Stokes equations, which requires the specification of boundary conditions similar to (5)–(7) together with appropriate initial conditions and to allow steady flow to develop with time. Such an analysis is, however, unwarranted since the flow processes in the series of experiments conducted on the wormhole at the low flow rates of 1.66 ml/min are close to Stokesian and occurs at a Reynolds number of approximately 12. This is approaching the upper limit of applicability of the linear Darcy flow as indicated by Bear.[34] (The variation of the Reynolds number along the effective path of the wormhole will be discussed in Sec. V.)

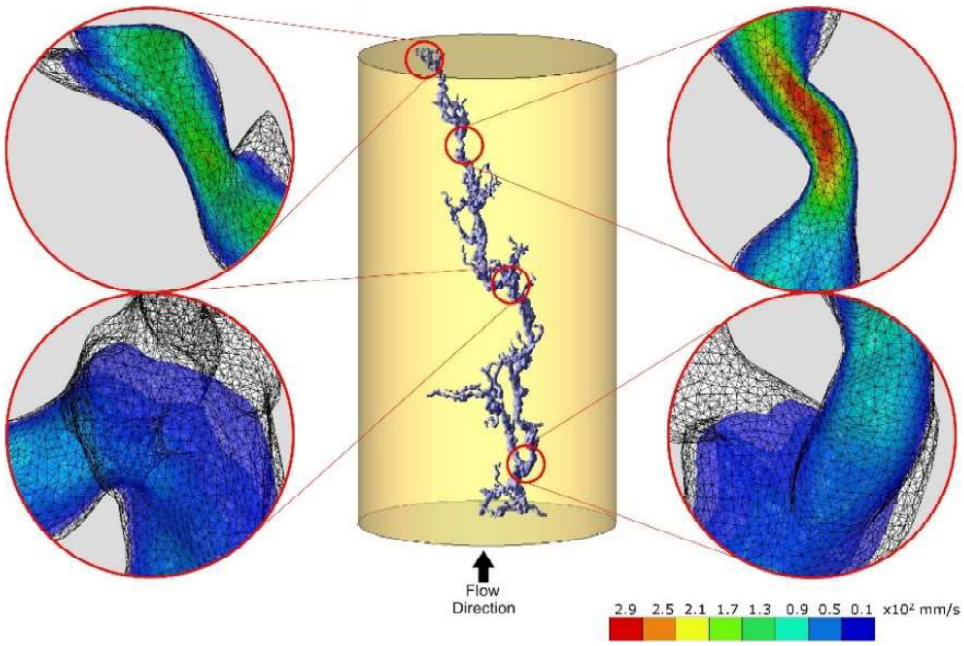

FIG. 7. Velocity field distribution at locations along the wormhole with details of the exterior mesh and the velocity field. Viewports show the range of velocities at various locations at a flow rate of 6.5 ml/min; stagnant zones are evident.

The permeability of one sample was measured using a steady state experiment and the values varied between 1.3×10^{-9} m^2 and 3.6×10^{-9} m^2, depending on the prescribed flow rate (Fig. 8). Comparatively, a computational simulation, using a finite element discretization involving approximately 1.3×10^6 tetrahedral elements, results in a wormhole permeability between 2.75×10^{-9} m^2 and 6.96×10^{-9} m^2 for the same range of flow rates. Permeability estimates obtained computationally by increasing the flow rates through the wormhole exhibit a trend consistent to that observed in the experiments. The discrepancy between experimental and computational estimates of wormhole permeability can be influenced by the geometry of the wormhole, which depends on the calibration technique used to determine the wormhole dimensions. There can be variability in estimating the *exact boundary* of the wormhole because the X-ray tomographic scans can be adjusted based on the gray scale threshold. To establish this influence, computations were repeated by either *enlarging* or *reducing* the geometry of the computational domain by ±5% in planes normal to the nominal axis of the wormhole.

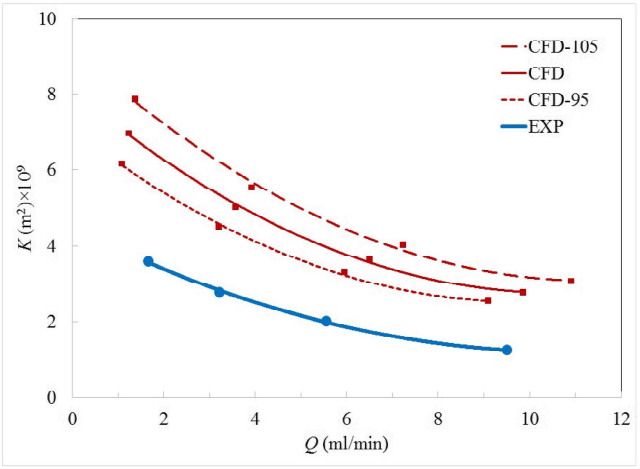

FIG. 8. Comparisons of computational (CFD) and experimental (EXP) estimates for wormhole permeability (wormhole cross-sectional area: 5.48 mm^2). Computational results for the scaled geometry of the flow domain are identified as CFD-105 (5% increase) and CFD-95 (5% decrease).

The permeability derived from computational simulations is illustrated in Fig. 8. Changes to the wormhole geometry only marginally altered the estimation of permeability; a consistent trend is observed in the variation of permeability with changes in the flow rate. The interpretation of the X-RT scans from the threshold technique is considered adequate. Other factors can contribute to the discrepancy between the experimental results and computational estimates, e.g., surface tension, particularly when fluid flow takes place in narrow aperture regions of the wormhole and temperature variations in the fluid supply, which can influence the fluid viscosity. These factors can influence the interpretation of permeability for the experimental results but are unaccounted for in the computational simulations. Although the irregular pattern of wormhole development results in large variations in the cross-sectional area along its path, an *average value* is used to estimate the wormhole permeability.

V. AN ALTERNATIVE APPROACH FOR ESTIMATING THE PERMEABILITY OF THE WORMHOLE

Although the concepts of the Stokesian slow viscous flow have been applied to the study of classical flow problems encountered in cylindrical tubes, annular regions, and flat parallel plates, their application to the estimation of permeability of tortuous paths can benefit from simplified approaches similar to those that were proposed recently in Ref. 35. The approach is based on pipe-flow-type assumptions where the flow is initiated by pressure gradients and certain approximations are invoked in terms of identifying the flow partitioning when the flow domain encounters rapid changes to its

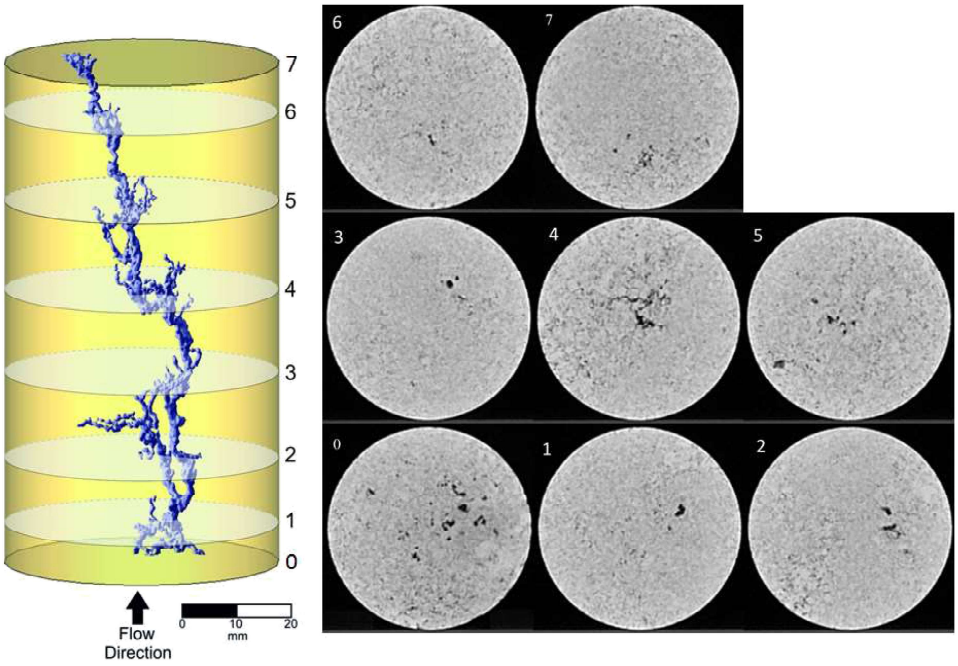

FIG. 9. The wormhole structure and X-ray tomographic images in selected cross sections.

geometry in terms of bends and flow path bifurcations. To interpret a measure of permeability from such calculations, however, it is necessary to invoke Stokesian flow assumptions to relate the flow rates through the wormhole to its permeability.

In estimating the Stokesian flow through the wormhole, all X-RT images were digitized and separate void areas in each image were determined. The wormhole structure and X-RT images in selected cross sections are shown in Fig. 9. Also, the X-RT images of the sample and the flow passages have been uploaded as a video.[36] As an example of the calculation process, Fig. 10(a) shows the X-RT image of the first cross section (the section closest to the entry location). The void areas of this image are shown as black spots inside the white area in Fig. 10(b). These void areas are used to develop the flow passages in the next step.

As an example, the first image has 26 separate void areas that have resulted in 26 separate passages (nodes 2-27 in Fig. 11) ramified from the input (node 1). For each void area, the cross-sectional area (A) and the perimeter (P) are estimated through digital techniques. The cross-sectional area of the void is calculated as the number of image pixels within

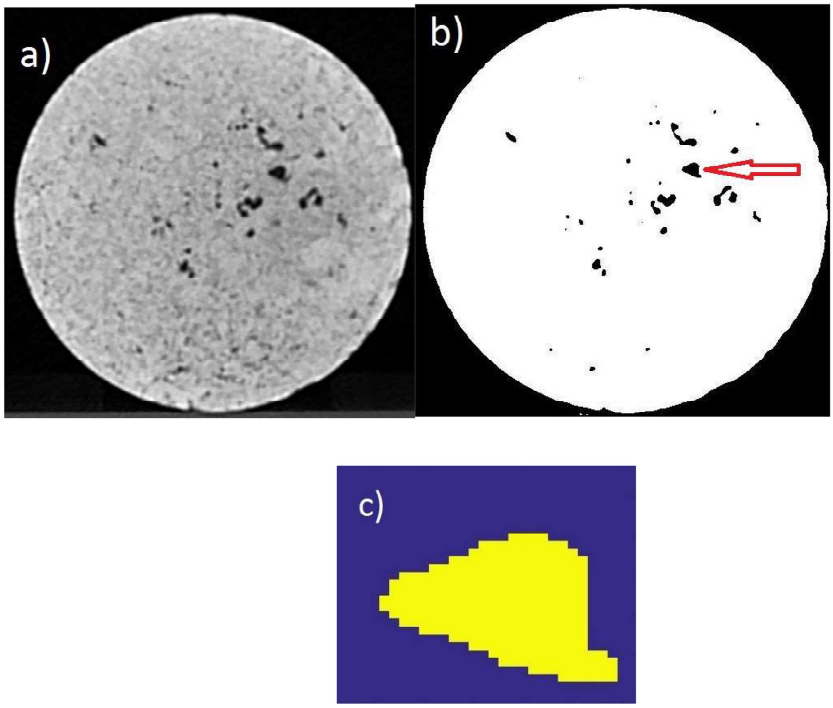

FIG. 10. (a) CT image of the closest cross section to the fluid entry location at the base of the test specimen, (b) the binarized version, (c) the magnified version of the spot specified in (b).

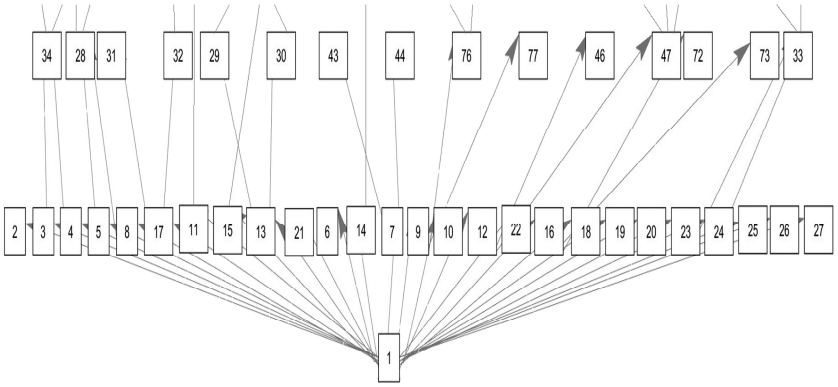

FIG. 11. The passages developed from the first X-RT images (the cross section closest to the fluid entry location).

the void area multiplied by the area of a pixel [i.e., the area of the yellow region in Fig. 10(c)]. The perimeter is estimated as the number of sides of the image pixels surrounding the void area multiplied by the length of a side [i.e., perimeter of the yellow region in Fig. 10(c)]. This estimation process does not necessarily result in the most accurate of approximations of the perimeter and needs to be revisited if the accuracy of the approach is to be further improved. The equivalent hydraulic diameter D_h for each void area is calculated from the relationship $D_h = 4A/P$. The ratio of the pressure drop (dp) to flow rate (Q) for each void area can be estimated as[31]

$$\frac{dp}{Q} = \frac{8\mu}{\pi(D_h/2)^4}h, \tag{8}$$

where μ and h are, respectively, dynamic viscosity of fluid and length of the image (i.e., the overall length of the wormhole divided by the overall number of images), respectively. To determine the pressure drop of the wormhole, passages of the flow have to be distinguished and the overall pressure drop to the flow rate ratio for each passage is calculated by summing this ratio for all the void areas that make up the passage. The flow rate distribution is then specified such that the pressure drop in parallel passages becomes equal.[35]

The passages obtained make up the wormhole and the connectivity of the void areas in successive images has to be analyzed. Starting from the first image (the cross section closest to the fluid entry location), each image is compared with the subsequent image (further away from the entry location) in order to develop the network of passages within the sample. If the void area x in the first image is projected on the next image and only covers the void area y of this image and the projection of void area y on the first image only covers void area x, these two void areas belong to the same passage and the dp/Q values are summed. On the other hand, if the void area x is also projected on void areas other than y, the passage that includes the void area x is divided. Similarly, if the void area y is projected on void areas other than x, two (or more) passages are combined. In each case, new passages have to be defined.

When the network of passages is developed [Fig. 12(a)], the dead-end passages (i.e., passages that are not connected to passages at locations remote from the entry point or close to the output surface) are identified and removed from the network [Fig. 12(b)]. An initial estimate for the flow rate distribution is then established based on the pressure drop estimations. Next, this initial flow rate distribution estimate is corrected using the Hardy Cross method.[37] The permeability of the sample can be determined from (2). Further details of this process are presented in Ref. 35.

The volume of the intact Indiana Limestone cylinder is approximately 196.35 ml. The volume of the entire wormhole created by CO_2-acidized flow is approximately 0.4773 ml, which represents approximately 0.243% of the total volume of the test specimen. The volume of the wormhole participating in the fluid flow process is approximately 0.3905 ml, which represents approximately 81.8% of the wormhole. By considering the precise geometry of the wormhole, the permeability of the sample is estimated using the combination of the pipe flow model and Stokes' flow assumption for interpreting permeability. This gives a permeability of approximately 3.65×10^{-9} m^2, which is sufficiently close to the measured permeability of 3.6×10^{-9} m^2 determined at the lowest flow rate 1.66 ml/min. If the overall geometry of the wormhole is increased by 5%, the predicted permeability increases to 4.44×10^{-9} m^2. It should be mentioned that the secondary influences of the cross-sectional shape of the passages are not considered and the velocity field due to the changes in the flow is assumed to be *fully developed* in all the cross sections (i.e., the void areas in the images). As a result, this interpretation of permeability is in fact based on Stokes' flow assumption but accounts for deviations of the flow path and the predicted permeabilities have to be considered as an accurate estimate of the permeability as the flow rate approaches zero (Fig. 13).

When the flow is assumed to be fully developed in the Stokesian flow regime, the correlation between the permeability and flow rate can be examined by disregarding the fully developed flow assumption. If the developing process of the flow is considered, the friction factor (C_f) can be corrected as proposed in Ref. 31,

$$C_f \,\mathrm{Re} \approx \frac{3.44}{\sqrt{\zeta}} + \frac{16 + 1.25/4\zeta - 3.44/\sqrt{\zeta}}{1 + 0.000\,212/\zeta^2}, \tag{9}$$

where Re is the Reynolds number based on the hydraulic diameter and $\zeta = (x/D_h)/Re$. The flow can be considered *fully developed* when $\zeta \approx 0.08$. The above relation was developed from the interpolation of pressure drop values for a wide range of flow aperture shapes. While Stokes' flow-based pressure is a linear function of the flow rate (i.e., permeability is

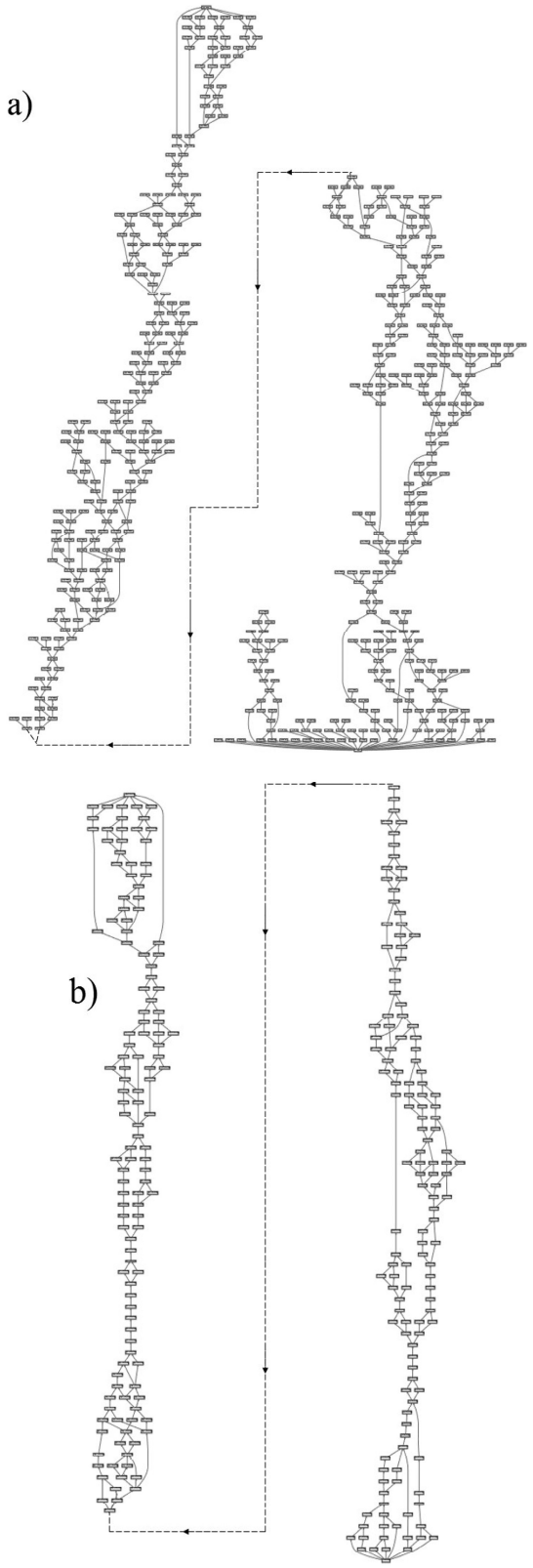

FIG. 12. (a) Complete network of passages. (b) Dead-end passages have been removed.

independent of the flow rate), the excess pressure drop of the developing flow [Eq. (9)] is not a linear function of the flow rate (i.e., permeability will vary with the flow rate), specifically because the entrance length (parameter ζ) is inversely related to the flow rate.

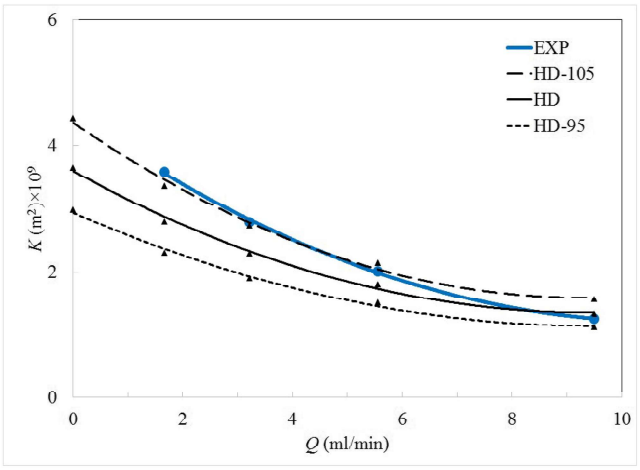

FIG. 13. Comparisons of Stokesian flow-hydraulic diameter (HD) and experimental (EXP) estimates for wormhole permeability (wormhole cross-sectional area: 5.48 mm^2). Computational results for the scaled geometry of the flow domain are identified as HD-105 (5% increase) and HD-95 (5% decrease).

To calculate the excess pressure drop during the developing process, the Reynolds number has to be determined. Figure 14 shows the Reynolds number variations for the length of the wormhole for the experimental flow rate of 1.66 ml/min in branches with the highest flow rates; the results suggest that the flow is in the laminar range but at a threshold for the Reynolds number that is close to the limit of applicability of the Stokesian flow (i.e., between 1 and 10[34]). At higher flow rates, the flow will remain in the laminar regime but the Reynolds number will surpass the limit conventionally associated with the Stokesian flow.

Using the Reynolds number variations, the excess pressure drop can be estimated from Eq. (9). Here, it is assumed that the flow needs to be re-developed when the Reynolds number difference between two successive images becomes greater than ten times the Reynolds number difference in the two previous images (resulting in the peaks and valleys seen in Fig. 14). The excess pressure drops for these developing flows are calculated by considering the ratio of the friction factor for the developing flow [Eq. (9)] to its developed flow counterpart (i.e., $C_f Re = 16$[31]). Figure 13 shows the permeability values calculated at different flow rates for the normal case and for the scaled geometries. Figure 13 suggests that if the excess pressure drops due to the flow developing process are considered, it is possible to predict the correlation between the permeability and flow rate with an acceptable accuracy. Figure 13 also shows that the model presented can predict the permeability of the wormhole more accurately than CFD results reported in Fig. 8.

The Reynolds number variations (Fig. 14) require specific attention: If the Reynolds number $Re = \rho U_{avg} D_h/\mu$ and hydraulic diameter (D_h) definitions are considered, the flow rate division in parallel passages does not result in equal Reynolds numbers (even if the hydraulic diameter remains unchanged along the entire length of the passage). The flow rate ratio in parallel passages is proportional to the ratio of hydraulic diameters to the fourth power [Eq. (8)] and the Reynolds number ratio is proportional to hydraulic diameters

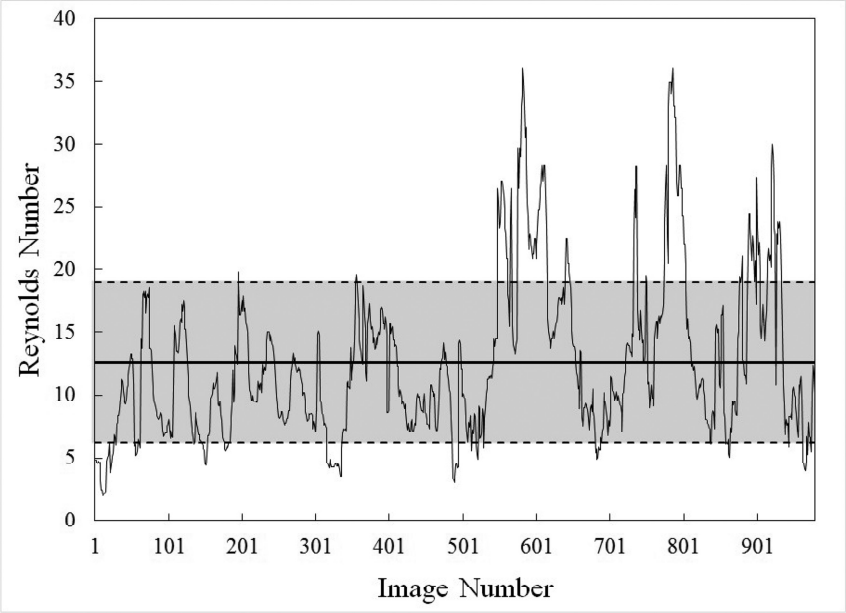

FIG. 14. Variations of the Reynolds number in the wormhole's length for a flow rate of 1.66 ml/min in branches with the highest flow rates. The average value and the standard deviation are also indicated in the figure.

to the third power. Also, while the Reynolds number is not a function of cross-sectional area (recalling that $U_{avg} = Q/A$ and $D_h = 4A/P$), it is an inverse function of the perimeter of the cross section (P) and, therefore, any rapid change in the cross section due to the division or combination of passages will result in a peak or a valley in the variations of the Reynolds number variation diagram (Fig. 14). It appears that the Reynolds number variations can be quantified and considered as a parameter that can be used to examine the correlation of the permeability and flow rate. The Reynolds number variations shown in Fig. 14 indicate that at the flow rate of 1.66 ml/min, the distribution of the Reynolds number along the active wormhole pathway gives an average value of 12.6, a root-mean-square of 14.1, and a standard deviation of 6.4.

VI. DISCUSSION AND CONCLUSIONS

The permeability experiments were repeated and the experimental results presented in the paper are reliable and accurate. The results of the CFD modeling that uses Stokes' flow tend to overestimate the permeability of the wormhole even though the mesh refinement which is given bounds to reflect the possible influences in the identification of the boundary of the wormhole obtained using the X-RT scans. This higher estimate for the permeability can result from several factors including (i) the assignment of a value for the viscosity of water, which could experience changes during the experiment, and (ii) the reliability of the boundary condition pertaining to zero fluid velocities at the surface of the wormhole as specified by boundary condition (7) in the paper. In the opinion of the authors, this latter condition could constrain the tangential flow velocities on the wormhole boundary, which could focus the flow towards the center of cross sections which finally could result in a lower overall pressure drop and contribute to an increased estimate of the wormhole permeability. The alternative to the boundary condition (7) on the wormhole surface is to replace the zero tangential velocity boundary condition with either (i) a zero shear traction boundary condition, (ii) a constant shear stress boundary condition, or (iii) a boundary layer solution, which will allow development of flow velocities that are consistent with what is most likely achieved in the experiment. These extensions will, however, require further studies that are relegated for future work. The approximate conduit base model tends to relax the shear stress boundary condition on the wall of the wormhole and this accounts for the better correlation between the experimental results. The CFD modeling can be extended to include the analysis of potential flow through the actual wormhole and the correlation is expected to be better, but the CFD modeling that uses Stokes' flow approach is advocated, since in geologic sequestration exercises, the fluids encountered can possess appreciable viscosity. These explanations for the possible departures between the experimental results, the CFD modeling, and the approximate conduit based model are based on the study of a single wormhole configuration and the studies need to be extended to other wormhole configurations to ensure that the discrepancies can be addressed through modifications proposed above and are warranted. As a final point, it should also be noted that the estimates from the three approaches are within the same order of magnitude and do not differ by several orders of magnitude.

The results for the permeability of a wormhole can be used to estimate the effectiveness of CO_2 storage if plausible values are assigned for the effective dimensions of wormholes created in a carbonate seam or vein present in a cap rock formation. As an *example*, consider CO_2 injection at a location with a cap rock thickness of 500 m and differential pressures that can create leakage through a wormhole spanning the entire cap rock thickness, at a constant differential pressure of 8.5 MPa. Assume that the CO_2-acidized water interacts with carbonate seams or veins in the cap rock creating wormholes with an average cross-sectional area of 0.01 m^2/km^2 of the storage region (i.e., an areal porosity of 0.0001%). The temperature-dependent estimates for density and viscosity of the injected CO_2 can be found in Ref. 31. The lowest

estimate of 1.3×10^{-9} m^2 for the permeability was used. (i) If the sequestered fluid is at a temperature of 50 °C, with a mass density of $\rho = 249$ kg/m^3 and dynamic viscosity of $\mu = 2.16 \times 10^{-5}$ Pa s, the fluid leakage from the wormhole will be approximately 3.23×10^5 m^3/yr. For an injection rate of 1 Mt/yr, this represents an annual leakage of 8.03%. (ii) If the sequestered fluid is at a temperature of 25 °C, with a mass density of $\rho = 789$ kg/m^3 and dynamic viscosity of $\mu = 6.88 \times 10^{-5}$ Pa s, the fluid leakage from the wormhole is approximately 3.21×10^5 m^3/yr. For an injection rate of 1 Mt/yr, this represents an annual leakage of 7.99%.

Similar calculations can be used to estimate leakage from other dissolution channel shapes.[13] Current guidelines proposed by IPCC (Intergovernmental Panel on Climate Change)[38] suggest that the leakage rates should not exceed 1% of the injected CO_2 over 1000 yr. Details of the *specific mechanisms* and *physical processes* that could contribute to leakage are scarce; the most widely cited mechanisms relate to abandoned wells with deteriorated seals and possible activation of existing fractures due to injection pressures. The current research suggests that wormhole development due to the interaction of acidized flows with any carbonate components in the cap rock should also be considered as a mechanism that will influence storage security and efficiency.

This research conclusively demonstrates that movement of CO_2-acidized water through calcium carbonate-rich rocks such as IL promotes the *rapid development of chemically eroded wormholes*. Within 24 h, all six intact samples of IL, irrespective of their initial permeability, developed wormholes resulting in an increase in the *effective permeability* in excess of *two orders of magnitude*. Since the dissolution process was localized, permeability of the wormhole cavity region itself increased by *six orders of magnitude* compared to the intact rock, leading to virtually unrestricted flow of injected fluids through the wormhole. Collateral effects of such erosion processes are (i) loss of efficiency of the sequestration potential of the storage formation; wormhole(s) can form conduits allowing injected CO_2 to bypass the storage area, rendering large areas of the formation unusable for sequestration. (ii) Transported dissolved carbonates can accumulate in remote regions where temperatures and pressures can promote precipitation, leading to a reduction in the permeability of the storage formation and possibly creating conditions for the development of hydraulic fractures. (iii) If substantial regions of the storage formation erode, distress to the caprock formation can occur due to loss of support, particularly when injection pressures are reduced. The process of wormhole collapse can threaten the integrity of the caprock. This research also investigated the influence of stresses applied to the skeleton of the porous medium and how this affected its susceptibility to wormhole generation. For the stress states investigated, there was no appreciable influence on the generation of the wormholes.

ACKNOWLEDGMENTS

This work was supported in part by research grants awarded by the *Natural Sciences and Engineering Research Council of Canada* (NSERC), *Carbon Management Canada* awarded to the first author, and an NSERC Postdoctoral Fellowship awarded to the third author. The authors are indebted to the reviewers for their important suggestions that lead to significant improvements to the paper.

[1] S. Bachu, D. Bonijoly, J. Bradshaw, R. Burruss, S. Holloway, N. P. Christensen, and O. M. Mathiassen, "CO_2 storage capacity estimation: Methodology and gaps," Int. J. Greenhouse Gas Control **1**, 430 (2007).
[2] J. Birkholzer and C. F. Tsang, "Introduction to the special issue on site characterization for geological storage of CO_2," Environ. Geol. **54**, 1579 (2008).
[3] B. J. McPherson and E. T. Sundqvist, *Carbon Sequestration and its Role in the Global Carbon Cycle* (American Geophysical Union, Washington, DC, 2013).
[4] A. P. S. Selvadurai, "Caprock breach: A potential threat to secure geologic sequestration of CO_2," in *Geomechanics in CO_2 Storage Facilities*, edited by G. Pijaudier-Cabot and J. M. Pereira (Wiley-ISTE, Hoboken, NJ, 2013), pp. 75–94.
[5] G. Pijaudier-Cabot and J. M. Pereira, *Geomechanics in CO_2 Storage Facilities* (Wiley-ISTE, Hoboken, NJ, 2013).
[6] J. E. Fessenden, P. H. Stauffer, and H. S. Viswanathan, "Natural analogs of geologic CO_2 sequestration, in carbon sequestration: Some general implications for engineered sequestration," in *Carbon Sequestration and its Role in the Global Carbon Cycle*, Geophysical Monograph Series, edited by B. J. McPherson and E. T. Sundquist (AGU, Washington, DC, 2013), pp. 135–146.
[7] R. B. Grigg, B. J. McPherson, and R. K. Svec, "Laboratory and model tests at reservoir conditions for CO_2-brine-carbonate rock systems interactions" in *The Second Annual Conference on Carbon Capture and Sequestration.* (Washington, DC, 2003), pp 1–17.
[8] D. Kramer, "Scientists poke holes in carbon dioxide sequestration," Phys. Today **65**(8), 22 (2012).
[9] M. D. Zoback and S. M. Gorelick, "Earthquake triggering and large-scale geologic storage of carbon dioxide," Proc. Natl. Acad. Sci. U. S. A. **109**, 10164 (2012).
[10] A. P. S. Selvadurai, "Heave of a surficial rock layer due to pressures generated by injected fluids," Geophys. Res. Lett. **36**, L14302, doi:10.1029/2009GL038187 (2009).
[11] A. P. S. Selvadurai, "Fluid leakage through fractures in an impervious caprock embedded between two geologic aquifers," Adv. Water Res. **41**, 76 (2012).
[12] V. Vilarrasa and J. Carrera, "Geologic carbon storage is unlikely to trigger large earthquakes and reactivate faults through which CO_2 could leak," Proc. Natl. Acad. Sci. U. S. A. **112**, 5938 (2015).
[13] L. E. Walle and E. Papamichos, "Acidizing of hollow cylinder chalk specimens and its impact on rock strength and wormhole network structure," in *49th US Rock Mechanics/Geomechanics Symposium* (American Rock Mechanics Association, San Francisco, CA, 2015), Vol. 4, p. 2500.
[14] J. Kim and A. P. S. Selvadurai, "Ground heave due to line injection sources," Geomech. Energy Environ. **2**, 1 (2015).
[15] A. P. S. Selvadurai and J. Kim, "Poromechanical behaviour of a surficial geological barrier during fluid injection into an underlying poroelastic storage formation," Proc. R. Soc. A **472**, 20150418 (2016).
[16] C. Noiriel, P. Gouze, and D. Bernard, "Investigation of porosity and permeability effects from microstructure changes during limestone dissolution," Geophys. Res. Lett. **31**, L24603, doi:10.1029/2004GL021572 (2004).
[17] J. G. Seo and D. D. Mamora, "Experimental and simulation studies of sequestration of supercritical carbon dioxide in depleted gas reservoirs," J. Energy Resour. Technol. **127**, 1 (2005).
[18] Y. LeGuen, F. Renard, R. Hellmann, E. Brosse, M. Collombet, D. Tisserand, and J. P. Gratier, "Enhanced deformation of limestone and sandstone in the presence of high PCO_2 fluids," J. Geophys. Res. **112**, B05421, doi:10.1029/2006jb004637 (2007).
[19] O. Izgec, B. Demiral, H. Bertin, and S. Akin, "CO_2 injection into saline carbonate aquifer formations I: Laboratory investigation," Transp. Porous Media **72**, 1 (2008).
[20] L. Luquot and P. Gouze, "Experimental determination of porosity and permeability changes induced by injection of CO_2 into carbonate rocks," Chem. Geol. **265**, 148 (2009).
[21] L. Luquot, O. Rodriguez, and P. Gouze, "Experimental characterization of porosity structure and transport property changes in limestone undergoing different dissolution regimes," Transp. Porous Media **101**, 507 (2014).

[22]A. Bauer, L. Walle, J. Stenebråten, and E. Papamichos, "Impact of acidizing-induced wormholes in chalk on rock strength," in *47th US Rock Mechanics/Geomechanics Symposium* (American Rock Mechanics Association, San Francisco, CA, 2013), pp. 2959–2964.
[23]P. Szymczak and A. Ladd, "Wormhole formation in dissolving fractures," J. Geophys. Res. **114**, B06203, doi:10.1029/2008jb006122 (2009).
[24]F. Huq, S. B. Haderlein, O. A. Cirpka, M. Nowak, P. Blum, and P. Grathwohl, "Flow-through experiments on water-rock interactions in a sandstone caused by CO_2 injection at pressures and temperatures mimicking reservoir conditions," Appl. Geochem. **58**, 136 (2015).
[25]L. W. Diamond and N. N. Akinfiev, "Solubility of CO_2 in water from −1.5 to 100 °C and from 0.1 to 100 MPa: Evaluation of literature data and thermodynamic modelling," Fluid Phase Equilib. **208**, 265 (2003).
[26]R. F. Scott, *Principles of Soil Mechanics* (Addison Wesley, New York, NY, 1963).
[27]A. P. S. Selvadurai and A. P. Suvorov, *Thermo-Poroelasticity and Geomechanics* (Cambridge University Press, Cambridge, 2016).
[28]Y. Bernabé, U. Mok, and B. Evans, "Permeability-porosity relationships in rocks subjected to various evolution processes," Pure Appl. Geophys. **160**, 937 (2003).
[29]C. E. Cohen, D. Ding, M. Quintard, and B. Bazin, "From pore scale to wellbore scale: Impact of geometry on wormhole growth in carbonate acidization," Chem. Eng. Sci. **63**, 3088 (2008).
[30]G. K. Batchelor, *An Introduction to Fluid Mechanics* (Cambridge University Press, Cambridge, 1967).
[31]F. M. White, *Fluid Mechanics* (McGraw-Hill, Boston, MA, 2008).
[32]A. P. S. Selvadurai, *Partial Differential Equations in Mechanics Vol. 2, The Biharmonic Equation, Poisson's Equation* (Springer-Verlag, Berlin, 2000).
[33]E. W. Lemmon, M. O. McLinden, and D. G. Friend, "Thermophysical properties of fluid systems," in *NIST Chemistry WebBook*, NIST Standard Reference Database Number 69, edited by P. J. Linstrom and W. G. Mallard (National Institute of Standards and Technology, Gaithersburg MD, 2016), p. 20899 (retrieved), http://webbook.nist.gov .
[34]J. Bear, *Dynamics of Fluids in Porous Media* (Dover Publication, New York, 1972).
[35]S. M. Rezaei Niya and A. P. S. Selvadurai, "The estimation of permeability of a porous medium with a generalized porous structure by geometry identification," Phys. Fluids **29**, 037101 (2017).
[36]See the video uploaded at https://www.mcgill.ca/civil/people/selvadurai/wormhole/connectivity.
[37]H. Cross, *Analysis of Flow in Networks of Conduits or Conductors* (University of Illinois Bulletin, 1936), Vol. 282.
[38]B. Metz, O. Davidson, H. De Coninck, M. Loos, and L. Meyer, *Special Report on Carbon Dioxide Capture and Storage* (Cambridge University Press, Cambridge, 2005).